Influence of silver nanoparticle additivation on Nd-Fe-B permanent magnets produced by Laser Powder Bed Fusion

Philipp Gabriel[1], Jianing Liu[2], Franziska Staab[3], Timileyin David Oyedeji[4], Yangyiwei Yang[4], Nick Hantke[5], Franziska Scheibel[3], Esmaeil Adabifiroozjaei[6], Oscar Recalde-Benitez[6], Leopoldo Molina-Luna[6], Ziyuan Rao[7], Baptiste Gault[7], Jan T. Sehrt[5], Konstantin Skokov[2], Bai-Xiang Xu[4], Karsten Durst[3], Oliver Gutfleisch[2], Stephan Barcikowski[1*], Anna Rosa Ziefuss[1]

[1] Technical Chemistry and Center for Nanointegration Duisburg-Essen (CENIDE), University of Duisburg-Essen, 45141 Essen, Germany

[2] Functional Materials, Institute of Material Science, Technical University of Darmstadt, 64287 Darmstadt, Germany

[3] Physical Metallurgy, Institute of Material Science, Technical University of Darmstadt, 64287 Darmstadt, Germany

[4] Mechanics of Functional Materials, Institute of Material Science, Technical University of Darmstadt, 64287 Darmstadt, Germany

[5] Chair of Hybrid Additive Manufacturing, Ruhr-University Bochum, 44801 Bochum, Germany

[6] Advanced Electron Microscopy Division, Institute of Material Science, Technical University of Darmstadt, 64287 Darmstadt, Germany

[7] Department of Microstructure Physics and Alloy Design, Max-Planck-Institut für Eisenforschung GmbH, 40237 Düsseldorf, Germany

* corresponding author: stephan.barcikowski@uni-due.de

Keywords:

Permanent magnetic properties
Hard magnets
Additive Manufacturing
Laser ablation in liquids
Rich finite element PBF-LB/M simulations
Recapture powder melting
Grain refinement

Abstract

Powder bed fusion of metals using a laser beam (PBF-LB/M) is an established additive manufacturing (AM) method that can be used to fabricate geometrically complex Nd-Fe-B magnets. However, the magnetic properties of Nd-Fe-B magnets manufactured by PBF-LB/M are typically inferior to conventionally produced magnets. To overcome this drawback, we modified the surface of the permanent magnet feedstock powder with 1 wt.% surfactant-free Ag nanoparticles (NPs) supporting the formation of relevant phases required for permanent magnetic performance to achieve a suitable micro- and nanostructure after AM. Our study is accompanied by finite element simulations, revealing the impact and dependency of process parameters during PBF-LB/M: a wide temperature field with a high-gradient profile in the front and on the bottom of an overheated region, implying a vast local heating/cooling rate and in-process high thermal stress. We found experimentally that the as-built part density can be affected by both the laser power and scan speed, causing a reduction in density as both parameters increase. The functionality and microstructural properties are also investigated via VSM, HR-SEM, EDX, EBSD, and exemplarily with HR-TEM-EDX and APT. Our study found that modifying MQP-S with Ag NPs increases the coercivity by approximately 20%, which we correlate to a decreased grain size. Additionally, we identified three distinct phases in the modified and unmodified samples, where Ag is primarily found in the intergranular and Nd-rich phases of the as-built parts. Overall, the study's findings contribute to the understanding of the factors that affect the quality and magnetic properties of Nd-Fe-B magnets fabricated through PBF-LB/M and provide valuable insights for further research in this area.

Introduction

New energy concepts are required for the future of industrial society, leading to an increasing emphasis on improving the efficiency of electricity generation and the progressive replacement of oil-based fuels in transportation by electric motors.[1] Strong permanent magnets are required to develop sustainable energy sources, electric vehicles, robotics, and electronics. Permanent magnets made from alloys, including elements from the group of Lanthanoids, in particular, rare-earth (RE) based materials like Nd-Fe-B magnets, are currently the strongest commercially relevant permanent magnets.[2] The large quantities of RE materials required to meet the increasing demand are hardly attainable, resulting in the industry's dependence on a limited number of supplying countries.[1, 3] Since their development in 1984 [4], scientists and corporations have been exploring methods to either enhance the magnetic properties of Nd-Fe-B magnets to maximize the utilization of RE materials or to develop techniques to minimize the quantity of RE required without compromising the mechanical and functional properties of the magnets.[5–7] Since the RE crisis in 2011, it has been emphasized that the growing demand and the current supply situation generate delivery shortages and possibly sharp price fluctuations.[1, 2, 7]

For rapidly solidified Nd-Fe-B permanent magnet materials, the ternary 2-14-1 phase is the primary component responsible for its overall good magnetic properties [8]. However, a second phase is required to decouple the 2-14-1 grains. In the case of rapidly solidified Nd-Fe-B magnets, this crucial second phase is a thin paramagnetic Nd-rich layer surrounding the $Nd_2Fe_{14}B$ grains [9]. The chemical composition of the Nd-rich boundary layer is similar to the Nd:Fe eutectic [10], but this can be altered by incorporating elements into the alloy, which preferentially locate in the boundary phase. For example, Fuerst and Brewer [11] analyzed the capabilities of multiple elements (Cd, Cu, Au, Ir, Mg, Ni, Pd, Pt, Ru, Ag, and Zn) to improve the magnetic properties of Nd-Fe-B magnets. They showed that especially the diamagnetic transition metals (Ag, Cu, Zn) can enhance the coercivity significantly.

In addition and to address the challenge of increasing demand for permanent magnets further, researchers are currently exploring their production through Additive Manufacturing (AM).[2] AM allows to create geometrically intricate and near-net-shaped parts, reducing the material requirements and shaping the magnets according to their functional requirements.[2] Here, producing fully dense and textured Nd-Fe-B magnets (similar to sintered magnets) without any non-magnetic binder volumes (required for

polymer-bonded magnets) is preferred to attain optimal magnet properties.[2] Powder bed fusion of metals using a laser beam (PBF-LB/M) is one of the most prominent AM techniques, which does not require binders. It is already used for many different alloys and applications since it enables small series production of fully dense metallic parts with high geometrical freedom, good dimensional accuracy, and reasonable surface finish.[12–15] PBF-LB of commercial Nd-Fe-B magnet micropowders has already been studied in the literature, mainly focusing on laser processing parameters and their correlation to mechanical or magnetic properties.[16–28] It has been reported that direct energy deposition[29] or PBF-LB/M[21] of the commercially available Nd-Fe-B micropowder[30] (called MQP-S, see methods section for details) may cause the decrease or even absence of a hard magnetic phase. A recent study conducted by Tosoni et al. [23] showed that the high cooling rates utilized in PBF-LB/M are advantageous for functional materials like Nd-Fe-B. This is evidenced by the micro- and nanostructures characterized in the as-built parts, which are crucial for achieving good permanent magnetic performance.[5]

Note that Kusoglu et al. [12] and Martin et al. [31] showed that nanoparticle additivation of feedstock powder could even intensify the positive effect of PBF-LB/M on the microstructure of the as-built part as they offer further nucleation sites, resulting in finer, more equiaxed grains. However, both groups focused on PBF-LB/M of Al-based powder feedstocks, and, to our best knowledge, there is no such reference for PBF-LB/M of nano-additivated Nd-Fe-B powder feedstocks. Nonetheless, it is important to note that the nanoparticles (NPs) used in PBF-LB/M must be devoid of chemical precursors typically present after wet-chemical synthesis, as they can negatively impact the flow characteristics of powder feedstocks during the process.[32, 33] Moreover, organic residuals or colloidal stabilizers bear the risk of creating gases by laser vaporization and may cause unwanted balling effects, as has been shown for laser direct-writing of stabilizer-containing Ag microparticle inks.[34] Unlike wet chemical methods, laser ablation in liquids (LAL) does neither require chemical precursors nor organic surfactants.[35] The pulsed laser system is focused on a solid metal target submerged in liquids removing material from the target surface with the removed material being collected in the surrounding liquid forming a colloidal dispersion of NPs.[35]

In this study, we additivated 1 wt.% (equivalent to 0.1 vol.%) of Ag NPs to the surface of Nd-Fe-B MPs to receive a modified powder feedstock for PBF-LB/M. Ag additions

to Nd-based magnets have been shown to benefit from the positive impact of Ag on their functional properties during conventional sintering.[36, 37] The authors found that adding Ag increases the volume fraction of the Nd-rich phase in the magnets. The Ag addition to the magnetic MPs also improved the fracture toughness[38], indicating its positive effect on mechanical properties. With Ag having a lower melting point than the Nd-Fe-B, it is melting rapidly and possibly filling open spaces in the loosely packed powder layers of the PBF-LB/M process, leading to a higher packing density, which positively affects the final part density[39] and hence the magnetic performance. Grain boundary infiltration with low melting point eutectic alloys, such as $Nd_{50}Tb_{20}Cu_{30}$ used by Huber et al. [20], to enhance the coercivity of MQP-S powder processed via PBF-LB/M using very low VED of 0.21 J/mm³ to 1211 kA/m, but at the cost of increasing the RE-content and reducing the volume fraction of the 2-14-1 phase and hence decreasing the remanence to 0.39 T.

Note, that none of the previous research studies utilized Ag NPs in combination with PBF-LB/M techniques. Therefore, we examine the combined beneficial effects of Ag nanoparticles and PBF-LB techniques on the functionality of permanent magnets based on Nd-Fe-B. Thereto, we examined how the PBF-LB/M process affects the permanent magnetic characteristics of as-built parts based on Nd-Fe-B. Moreover, we analyzed the impact of Ag NPs during PBF-LB/M at different process parameters (laser power, scan speed) on the as-build part density and microstructure. Finite element PBF-LB/M simulations accompany the experimental part of this study to recapture powder melting of Nd-Fe-B-based feedstock.

.

Materials and Methods

This study used a gas-atomized Nd-Fe-B-based isotropic powder manufactured by Magnequench (Tuebingen, Germany). The powder is commercially known as MQP-S-11-9-20001 (hereafter referred to as MQP-S) with a nominal chemical composition of $Nd_{7.5}Pr_{0.7}Zr_{2.6}Ti_{2.5}Co_{2.5}Fe_{75.4}B_{8.8}$[30], which we sieved to a particle size distribution (PSD) of 20-64 µm, better resembling the typical PSD for the PBF-LB/M process, with the arithmetic mean $\mu_d = 32\,\mu m$ and standard deviation $\sigma_d = 8.67\,\mu m$. A surface-weighted size distribution can be found in Figure S1A in the supporting information (SI). It has a spherical morphology and is generally used for manufacturing bonded magnets, particularly by injection molding, extrusion, and calendaring where it achieves a coercivity of up to H_{cl} of 730 kA/m and a remanence B_r of 0.75 T according to the supplier's material datasheet.[40] Characterization of the powder size distribution and morphology was performed by scanning electron microscopy (SEM, Philips ESEM-XL30 FEG, 20 kV). The powder density was measured using a pycnometer (Borosilicate glass 3.3. DIN ISO 3507, BRAND 25 ml type Gay-Lussac).

Laser-based synthesis of Ag NPs and surface modification of the MQP-S feedstock

The Ag NPs were prepared by laser ablation in liquids (LAL) [35], where the laser beam ablated the surface of a bulk Ag target (20mm (width) x 80mm (length) x 2mm (thickness)), using an ns-pulsed laser (Innoslab, IS400-1-L, Edgewave GmbH, Würselen, Germany) at 145 W average output power. The laser wavelength was 1064 nm, with a laser pulse duration of 8 ns and a pulse repetition rate of 5 kHz (resulting in a pulse energy of 29 mJ). A galvanometer scanner (intelliSCAN-20, Scanlab AG, Purchheim, Germany) with a scan speed of 2 m/s and an F-theta lens focusing optics f = 100 mm was employed. A flow-through ablation chamber was used (as described in [41]. The ablation was done in 0.1 µg/L NaOH, which is known to be a good inorganic stabilizer.[42] The hydrodynamic diameter of the synthesized Ag NPs was measured by analytical disc centrifugation (ADC, CPS instruments) at a centrifugation speed of 24,000 rpm with a lower detection limit of 5 nm (Figure S1B in the SI).

The additivation of 1 wt.% of Ag NPs on the MQP-S micro powders' surface was performed by mixing the MQP-S powder directly with the colloid, which corresponds to a theo. covered surface of 50%, or half a monolayer (see Figure S1C in the SI). To force diffusion-controlled supporting, the pH value of the Ag NPs was lowered to 7,

which is a value between the isoelectric point of MQP-S and Ag NPs, but still high enough to avoid a negative effect on the metal powder surface. After the NPs were successfully deposited on the surface of the MQP-S, the modified feedstock was separated from the liquid by centrifugation (4,000 rpm at 10˚C for 15 minutes) and dried in a vacuum oven at 40˚C.

Sample production via powder bed fusion using a laser beam (PBF-LB/M)

A TruPrint 1000 by Trumpf (laser beam wavelength at 1070 nm and a focal diameter of 30 µm) was used as the PBF-LB/M system for sample production under Ar atmosphere. Cylindric samples with a diameter of 5 mm and a height of 5 mm were fabricated directly on a build platform composed of C45 steel. The volumetric energy density (VED) is calculated as follows:

$$VED = \frac{P_L}{v_s \cdot H \cdot LT}$$

with P_L being the laser power, v_s being the scan speed, H being the hatch distance and LT being the layer thickness. It is a synthetic parameter typically used in [J/mm³], which cannot be considered an absolute indicator due to its limit in capturing the complexity of the melt pool physics of PBF-LB/M, as sufficiently discussed in the literature [43]. However, VED found its utility in explaining the effects of process parameters on part properties like surface roughness, hardness, and porosity characteristics.[44] As it is a value often used in the context of PBF-LB/M, it is applied in this study to enable a comparison of our results with published data of other groups who manufactured magnetic samples via PBF-LB/M. Additionally, the VED is employed in the following sections to classify the impact of adding Ag NPs produced with the same parameter combinations. Because MQP-S is not optimized for high melting temperatures (tends to lose hard magnetic phase), we performed PBF-LB/M at moderate process conditions of VEDs between 51.9 and 75.4 J/mm³. These have been adjusted via the laser power in increments of 4 W, ranging from 70 to 78 W, as well as varying the scan speeds in increments of 350 mm/s, ranging from 2300 to 3000 mm/s. All samples were manufactured with a constant layer thickness of 30 µm and a constant hatch distance of 15 µm.

Analysis of the as-built parts' functional properties

To determine the magnetic performance of the manufactured samples, isothermal magnetization measurements were performed on samples in the as-build state without further post-processing steps using a physical property measurement system - vibrating sample magnetometer (PPMS-VSM, Quantum Design PPMS-14) at room temperature under an applied magnetic field of up to ±3 T. To confirm our results, we analyzed three different samples per feedstock (modified and unmodified) produced with these parameters, leading to three fitted lines per feedstock.

Analysis of the as-built parts' density and microstructure

We measured the density following DIN EN ISO 2738 for open porosity samples. The chemical and structural characterization of the as-build parts was carried out via scanning electron microscopy (SEM, Tescan Mira3) by backscattered electron (BSE) imaging and energy-dispersive X-ray spectroscopy (EDX) point scans and mapping using 20 kV acceleration voltage. To obtain the grain orientation, electron backscatter diffraction (EBSD) analyses were performed using a FEG-SEM (Tescan Mira3), operating at 30 kV with a step size of 40 nm. For each sample, two maps with an area of 24 x 54 μm^2 have been analyzed. To improve the indexing rate, a neighbor pattern averaging, and re-indexing (NPAR) post-processing routine was applied using the software OIM Analysis 8.6 (EDAX). Grains are induced only from a minimum number of 10 pixels. More in-depth nanostructural analysis has been carried out exemplarily on the Ag-additivated, 71.5 J/mm^3 VED sample, using TEM-EDX map and point-scans as well as imaging high-resolution transmission and scanning transmission electron microscopy (HR-TEM and STEM, JEM ARM 200F, by JEOL, combined with the EDX-detector JED 2300T, by JEOL). Furthermore, atom probe tomography (APT) via a local electrode atom probe (LEAP 5000, by Cameca Instruments) was used to investigate the Ag distribution in a selected surface area of an Ag-NP modified PBF-LB/M produced sample.

Results and Discussion

We performed a process parameter screening and determined an applicable parameter window of laser power P_L ranging from 70 to 78 W, and scan speed v_s, from 2300 to 3000 mm/s (noted in the form of $\{P_L, v_s\}$ hereinafter), with a layer thickness of 30 µm and hatch distance of 15 µm. Note that with too low energy inputs, the parts are expected to build up fragmented due to insufficient fusion of the powder particles. In contrast, too high energy inputs lead to the delamination of printed layers due to insufficient heat transfer from the heat zone to the build plate.

Here we manufactured 15 sample parts (see materials and methods sections, as well as photographs in Figure S2 in the SI) by subjecting the unmodified feedstock to PBF-LB/M while adjusting the laser power (P_L) and the scanning speed (v_s). Figure 1A shows the resulting relative as-build part density for unmodified powders, which ranges from 80 – 86%, dependent on the applied VEDs (52 – 75 J/mm³). As the material is very brittle, it is likely to have fully dense regions in one part of the sample but large porosity in others. At the same time, residual cracks and structural defects could cause a general reduction in part density. Our findings indicate that the density of the part can be affected by both the laser power and scan speed, causing a reduction in density as both of these parameters are increased. While an increase in v_s leads to lower part densities was anticipated because of a reduced energy input [16, 22], the impact of P_L on the density seems more complex. Note that both parameters are influenced by interdependencies with other process parameters (like point distance, hatch distance, exposure time, and layer thickness), as shown by multiple studies [16, 22, 45, 46]. Therefore, all those parameters have been kept constant in this study.

Tosoni et al. [23] observed that higher laser power leads to a wider melt pool in Nd-based alloys, which is typically assumed to have a beneficial effect on the density of the final part after resolidification (e.g., Figure 20 in ref[14]). However, they found that solidification in wider melt pools can be slower, which can hurt the microstructure of the as-built part.[23] Brown et al. [47] investigated the correlation between part density and laser power on Nickel Alloy 625. They found that average bulk density increased non-linearly with increasing energy density values which contradicts our findings in Figure 1A.

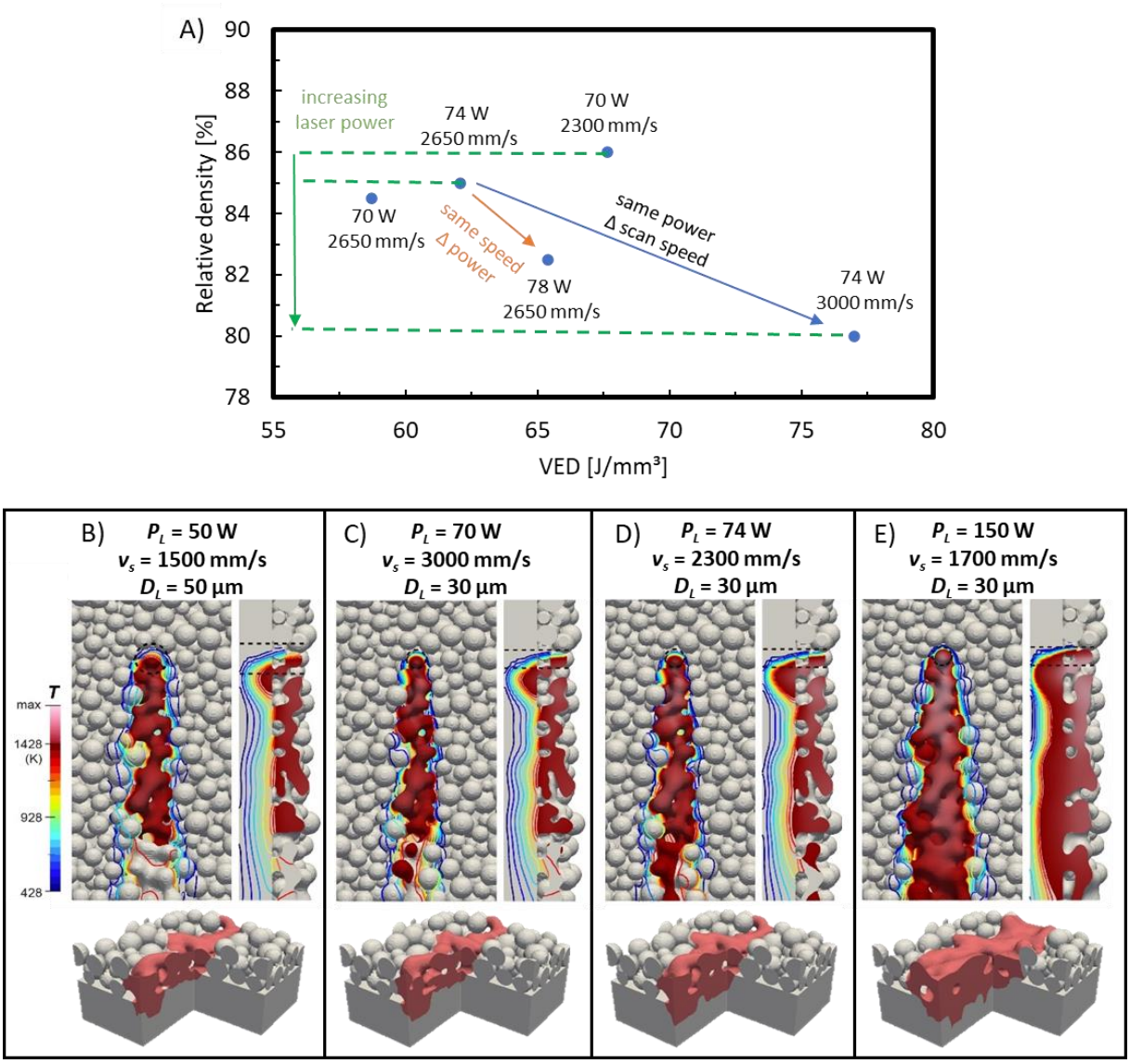

Figure 1 A) Plot of the Archimedean density determined on as-build-parts in dependence of the applied VED (adjusted by changing the laser power and scan speed) during PBF-LB/M processing, B-E) show simulations with varying laser power and scan speed at the time point when the laser center locates at x = 310 µm. Overheated regions, where T > T_m, are drawn with a continuous color map, while areas with T ≤ T_m are shown as isotherms. The laser spot characterized by D_L is also indicated by dotted lines within the simulated melt tracks.

To explain these contradictions, we investigated the effects of different process parameters on the melt pool behavior by recapturing the powder melting in finite element simulations of the PBF-LB/M process (Figure 1B-E). Further information on the modeling, including the VED values, can be found in section 3 of the SI. The processing parameters, notably P_L, v_s, and the laser diameter D_L (noted in the form of $\{D_L\}$ hereinafter), are chosen as input parameters for the simulations of two selected combinations based on the experiments in this work (Figure 1C and D) and compared with two selected cases from literature as reference (Figure 1B [45] and E [17]).

In Figure *1*Figure 1B-E, the overheated region where $T > T_{\mathrm{m}}$ is noted with a continuous colormap. Other regions with $T \leq T_{\mathrm{m}}$ are indicated with temperature isotherms. Particles are fully molten within the overheated region, while partial melting or sintering must be considered in the other regions. The tendency of surface energy reduction drives mass transfer, notably, the surface diffusion and the localized melt flow, from the convex to the concave point. Consequently, in regions with $T \leq T_{\mathrm{m}}$, even though there is no melting, the temperature is high enough to induce solid-state sintering as observed via the formation of necks between adjacent particles. Comparing the different scenarios revealed that if the D_{L} is held constant (C to E: D_{L} = 30 µm), increasing P_L or decreasing v_s leads to greater heat accumulation at the beam spot, ultimately resulting in a more pronounced overheated region. Whereas the larger D_{L} focuses the laser energy on a larger area (2D) or volume (3D), which leads to a wider melt pool and more powder particles being in the heat-affected zone, but this can lead to faster cooling as the heat transfer can occur over a larger area or volume, respectively. The different values of P_L and v_s, can be seen in the simulations by more particles in the beam path colored grey (corresponds to build volume temperature) compared to the other simulations. For fixing v_s, high P_L can lead to tarnished part quality. This is mainly due to the reduction in part density via accompanied evaporation or even via furious vaporization that introduces extra pores by keyholing. Increased residual stress is also expected due to enhanced local temperature gradient around the melt pool. Therefore, the relationship between P_L and part density in PBF-LB/M is only limited and applicable for producing Nd-based feedstocks via PBF-LB/M and may depend on various factors, such as the D_{L}, v_s, powder bed properties, and process parameters.[48] It is noteworthy that the thermal-microstructural simulations were performed with unity absorption. In other words, a complete power absorption within the laser spot was assumed, whereas such absorption has been shown to depend on P_L and D_{L} [49, 50]. High-fidelity ray tracing simulations also unveiled the positive linear correlation of the absorptivity on P_L within a low energy density range. When P_L is high enough to create increased melt pool depth, more absorption events are expected due to the enhanced accommodation of reflections by the melt pool [50]. Such effect is, however, tentatively disregarded in the presented thermal-microstructural simulations for variable control and should be explicitly implemented in future works.

Besides these factors, the influence of the material properties is highly relevant, especially in functional materials. The powder material's thermal properties are one

factor that directly affects the observable process features and hence the microstructure evolution of the material, together with the powder bed packing density, specific energy input, and laser diameter.[50–52] For instance, melt pool size strongly relates to the powder materials' thermal conductivity.[53, 54] The thermal conductivity of Nd-Fe-B is relatively low when compared to other typical alloys used in PBF-LB/M processing (comparison in Table 1 in Ref. [16]), which leads to relatively low homogenized thermal conductivity in the powder bed with the same powder size distribution.[52]

In summary, the simulations of Nd-Fe-B powder melting processed via PBF-LB/M show a temperature field with a high-gradient profile on the front and the bottom of the overheated region, implying a vast local heating/cooling rate and in-process high thermal stress for all sets of processing parameters considered, as seen in Figure 1B-E. Processing Nd-based feedstock with too high P_L not only negatively affects part quality by reducing its density, as mentioned before, but also leads to an elongated microstructure, as shown in the compared studies [17, 45]. Micro-cracks and lack of fusion pores might cause the absence of anisotropy if they reduce the heat transfer in the building direction and influence the thermal gradient.[26] On the other hand, at appropriate VED, cubes were successfully printed by PBF-LB, with sintering contributing to the printing process. In the next step, we investigated the functional properties to find further correlations with the printing parameters.

Functional properties of the as-build parts

The second quadrant of the resulting hysteresis loops is shown in Figure 2A (the full hysteresis loops are shown in Figure S4 in section 4 of the SI) for as-build parts (without further heat treatments) produced from pure MQP-S and the silver NP-modified feedstock variant at different VEDs between 62.0 J/mm^3 and 77.8 J/mm^3. Figure 2B shows the hysteresis loops of the samples processed at the same VED of 71.5 J/mm^3 (74 W and 2300 mm/s), resulting in the highest magnetic properties for the modified feedstock (green) with a coercivity H_{cl} of 935 ± 6 kA/m and a remanence B_r of 0.63 ± 0.01 T, and for the unmodified feedstock (orange) with H_{cl} of 769 ± 59 kA/m and B_r of 0.58 ± 0.02 T. We found that the NP modification of MQP-S significantly increases the coercivity by roughly 20 % without negatively affecting the remanence. Also, the deviation of the measured properties is reduced, and the squareness of the hysteresis loops is slightly improved. Note that we expected the inclusion of Ag to reduce the

remanence as it is a diamagnetic material. Also, the results at a VED of 64.8 J/mm³ are worth noting, as the unmodified sample only reached roughly 175 kA/m, whereas the corresponding modified sample led to roughly 750 kA/m. But as the unmodified sample only shows a few measurement points in the second quadrant, the results are too indecisive to conclude. Although not leading to the highest magnetic properties, the significant increase in magnetic properties after adding Ag NPs must be investigated further.

Comparing our results with literature data on PBF-LB/M of MQP-S, the highest achieved coercivity for the NP-modified sample amounts to 935 kA/m This is, to our best knowledge, the highest coercivity that was found for PBF-LB/M proceeded MQP-S-based feedstocks without heat treatments even exceeding literature values as shown in Figure 2C and D. Note, that significant alterations of MQP-S or different compositions of Nd-Fe-B feedstock have not been included in the comparison as they lack comparability. Plotting the VEDs versus the achieved magnetic properties of references (labeling as applied in this study and described in section 5 of the SI) and our results shows possible trends. Still, as the data pool is insufficient, we refrain from drawing a guide to the eyes. Here, the lower orange circle indicates the achieved properties with pure MQP-S, and the upper green triangle indicates the achieved results by adding 1 wt.% Ag NPs, where both have been produced at the same VED of 71.5 J/mm³. Wu et al. [16] reached a slightly higher remanence of 0.65 T, which could be connected to their investigation of different hatch distances potentially influencing the resolidification rate of neighboring melt pools leading to slightly better grain alignment and texture. Furthermore, as the same VEDs could be achieved by completely different process parameters, Figure S5 in the SI shows the applied laser power and scan speed values of the references, which have been used for comparison here.

Overall, the addition of 1 wt.% Ag NPs lead to an increase in coercivity by roughly 20% comparing the modified and the unmodified samples produced via PBF-LB/M at the same process parameters of 74 W and 2300 mm/s (leading to a VED of 71.5 J/mm³). To better understand how the process parameters and the addition of Ag in the form of NPs leads to these magnetic properties, its effect on the microstructure has been investigated via BSE-SEM, EDX, and EBSD and exemplarily with HR-TEM-EDX and APT in the next steps.

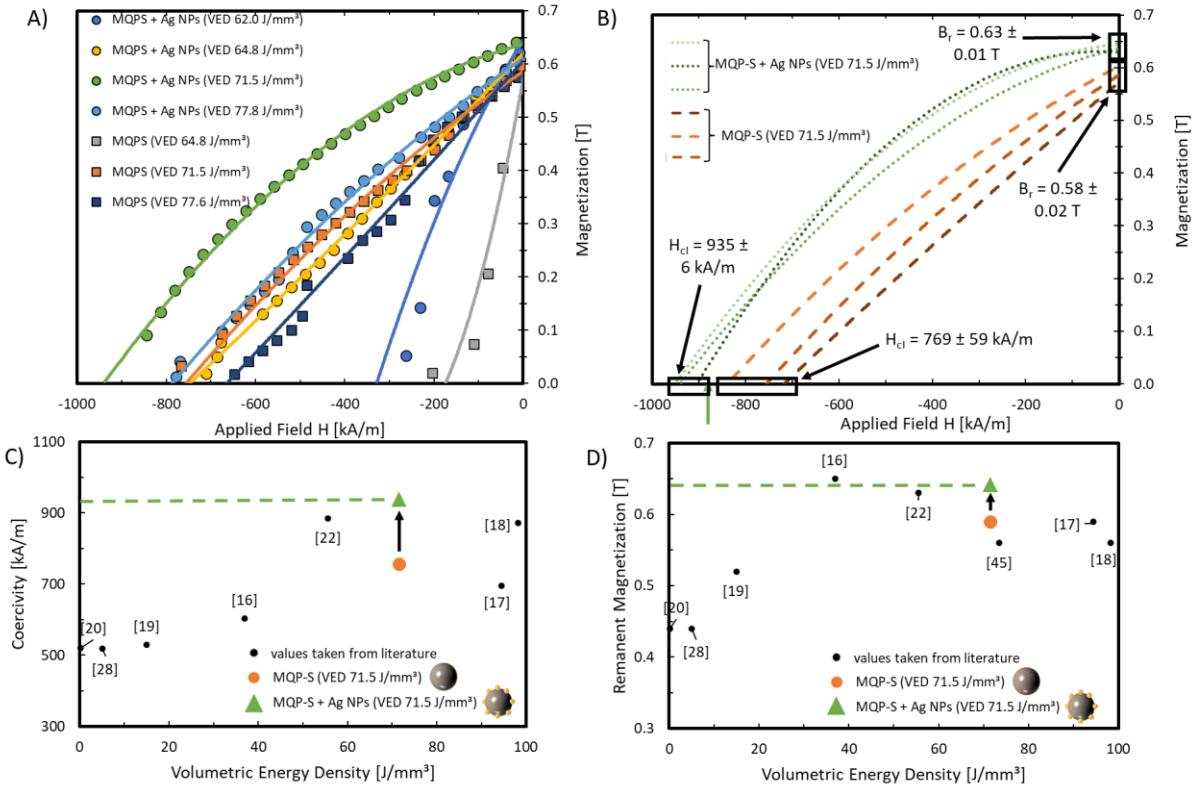

Figure 2 Second quadrant of hysteresis loops of A) MQP-S with and without Ag NPs for different VEDs tested in our study and B) direct comparison of three individual samples of MQP-S without (orange curves) and with 1 wt.% Ag NPs (green curves) after PBF-LB/M using Volumetric Energy Densities (VED) of 71.5 J/mm³. C) - D) VEDs and achieved magnetic properties of references (labeling as applied in this study and described in Table S2 in the SI) in comparison to our best results, where the lower orange circle indicates the achieved properties with pure MQP-S and the upper green triangle indicates the achieved results by addition of 1 wt.% Ag NPs. Note: no results achieved by heat treatments after the PBF-LB/M process are included. Some references did not state all required process parameters or magnetic properties and could therefore not be included in all curves.

Microstructural analysis: grain size, grain size distribution, grain orientation, and composition

We examined the microstructure of the two best-performing parts (Ag NP-modified and unmodified), which have been produced at a VED of 71.5 J/mm³ (74 W and 2300 mm/s). We found no significant differences after analyzing SEM images at low magnification of both samples, as shown in Figure 3. However, we found large pores in both samples and only partially molten microparticles may contribute to the previously discussed reduced samples' densities of roughly 80 – 86%.

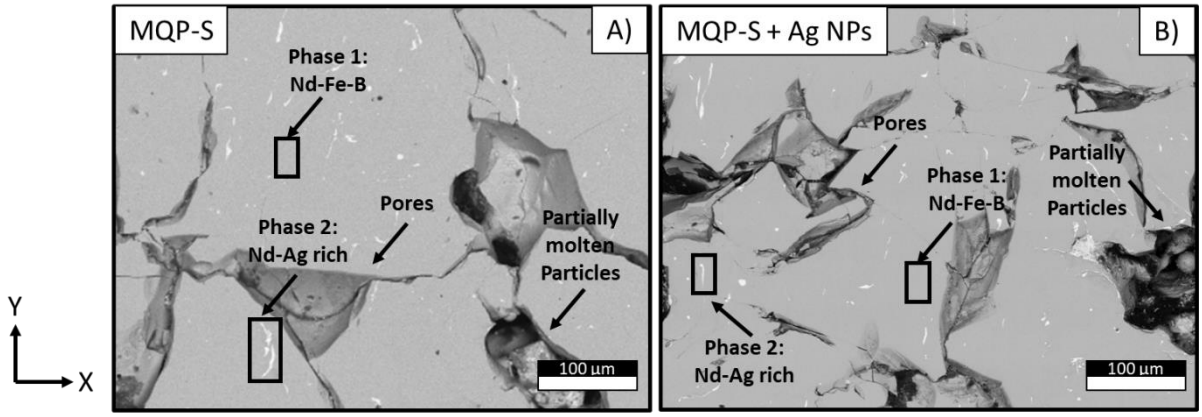

Figure 3: BSE-SEM images of horizontal cross-sections of the as-build parts produced by PBF-LB with A) unmodified MQP-S feedstock powder and B) the surface-modified MQP-S + Ag NP feedstock powder.

Two distinct regions (bright and grey) can be identified. Possibly, the bright regions were aligned lengthwise with the building direction, which may be more noticeable in the unmodified feedstock (as shown in Figure 3A). Still, this observation could not be conclusively verified through our measurements. SEM-EDX at higher magnifications of a sample with Ag NPs, shown in Figure 4, revealed that the bright regions contain mainly Nd, whereas the grey regions contain mainly Fe. The EDX analysis of a sample without modification is shown in Figure S6 in the SI, which was fairly comparable to the modified sample.

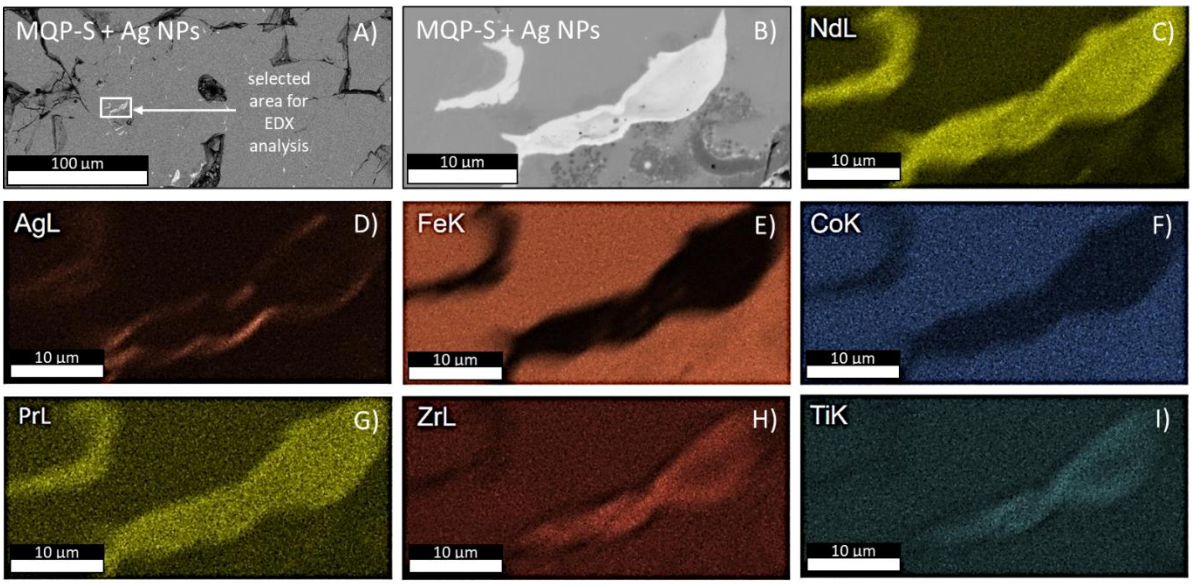

Figure 4 Analysis of the chemical composition and distribution of the Nd-rich phase (bright region) of a PBF-LB-printed sample of MQP-S modified with 1 wt.% Ag NPs. A) BSE-SEM image showing the selected region for the EDX analysis. B) BSE-SEM image of the bright region at higher magnification. C–I) EDX mappings showing the

elemental distribution of the main elements of MQP-S and Ag. Corresponding data for the unmodified powder are shown in section 6 in the SI.

The higher resolution in Figure 4A, combined with the elemental mappings, revealed a third phase containing the highest amount of Ag (2.76 wt.%), which surrounds the Nd-rich grains (bright contrast). The elemental composition of the combined EDX mappings (shown in Figure 4B-H) is listed in Table 1. Note that larger, more rounded Nd-rich grains (as we assume for the sample in Figure 4A) are typically oxides. In contrast, smaller, angular regions and thin layers in the $Nd_2Fe_{14}B$ grain boundaries are metallic.[55] The EDX analysis identified the bright region (phase 1) in the BSE SEM images as the Nd-rich phase, containing mainly the RE elements Nd (68.49 wt.%) and Pr (8.47 wt.%) as well as larger amounts of Zr (9.71 wt.%) and Ti (2.99 wt.%). In comparison, the matrix (Phase 2) mainly contains Fe (72.92 wt.%) combined with Nd (14.88 wt.%), which roughly fits the stoichiometric composition of the expected $Nd_2Fe_{14}B$ grains with some degree of additional Fe, which most likely is α-Fe, because this would be the usual case for nanocomposite, exchange coupled MQP-S feedstock[30]. $Nd_2Fe_{14}B$ resembling the matrix phase is caused by the magnification of the BSE-SEM image used for the analysis, which is insufficient to resolve the nanograins of the two $Nd_2Fe_{14}B$ and α-Fe phases. Nd-rich grains in the size of a few µm are known from sintered Nd-Fe-B magnets (see Figure 1 in [5]), but in Figure 3, the Nd-rich phase forms large regions of up to 40 µm forming macroscopic inclusions. Furthermore, the chemical composition of the intergranular phase (phase 3) surrounding the Nd-rich phase is interesting. This third phase consists mainly of Fe (41.49 wt.%) and Nd (42.30 wt.%) and traces of Co, Pr, Zr, and Ti. In the sample surface modified with Ag NPs a significant Ag concentration was detected both in the Nd-rich phase (1.21 wt.%), and the intergranular phase (2.76 wt.%), but Ag content in the matrix (phase 2) has been below the detection limit. Therefore, whether Ag is also distributed within the Fe-matrix remains uncertain. The alloy additives of Co, Ti, and Zr stabilize the growth of the magnetic phase by affecting the nucleation of the 2:14:1 phase and influencing the kinetics and thermodynamics of the solidification.[56] The Ag NPs might enhance this effect by gathering in the grain boundary phase during the fusion (or sintering) step and increasing the number of nucleation sites during the rapid cooling process steps of PBF-LB/M. Note, that repetitions of EDX measurements taken at further bright regions confirmed the first results and that Ag seems to surround all these grains.

Table 1 Elemental composition of the three main phases detected in Figure 4 of MQP-S with 1 wt.% Ag

Phase [wt.%]	Ag	Nd	Fe	Co	Pr	Zr	Ti
Phase 1 (bright) Nd-rich phase	1.21	68.49	9.00	0.12	8.47	9.71	2.99
Phase 2 (grey) $Nd_2Fe_{14}B$ + α-Fe phase	NA	14.88	72.92	3.33	1.83	4.41	2.21
Phase 3 Intergranular phase	2.76	42.30	41.49	1.65	5.37	4.76	1.68

HR-SEM at higher magnification (20,000x) of the modified and unmodified as-build part has been performed to investigate the effects of NPs modification on the grain shape and size (see Figure 5A, B). Here, the line(s) of dendritic-elongated grains through the entire image zone are typical for the PBF-LB/M process and are caused by the melt pool boundaries.[57] Due to the layer wise manufacturing technique, lower layers of the powder bed get (partially) remolten as the melt pool generated by the laser beam is intended to combine previous layers with subsequent layers. The heat accumulation and extended cooling periods enable crystal restructuring and grain growth. These chains are surrounded by significantly smaller grains (~200 – 500 nm) and are comparable in shape for both as-built parts. Our results are comparable to the findings of Bittner et al. [26], who achieved a heterogeneous microstructure containing a few coarse grains with a size of 250 nm embedded in a fine-grained matrix with a size of roughly 60 nm. The rapid cooling times of the PBF-LB/M process probably quenches the material, thereby limiting the grain growth (except for the before-mentioned regions of remelting), as known from the melt spinning process [58]. Although the dendritic-elongated grains caused by the melt pool boundaries appear unaffected by the addition of Ag NPs, the grains in the modified as-build part (as shown in Figure 5A, B) are smaller and outside the melt pool boundary region cannot be detected with the used SEM. During the PBF-LB/M process, the Ag NPs can be considered to co-exist in the melt pool in nanodroplets due to their lower melting point compared to Nd-Fe-B, which suggests disturbances in the melt pool flow and temperature gradients. Additionally, the melt pool during PBF-LB/M is affected by keyholing effects due to enhanced recoil effects from the high vapor pressure above the melt pool and the Marangoni effects due to the evident coupling between the melt flow and temperature

field with a high-gradient profile [50, 59]. The combination of these effects could explain the reduction in grain size because they strongly influence the stability of the nanodroplet-melt dispersion system. Due to a strong screening effect and thus elimination of the considerable inter-nanodroplets' repulsive force inside a molten metal, the Ag nanodroplets intrinsically possess the tendency to merge [60]. In that sense, these existing disturbances can redistribute the nanodroplets in the melt pool, i.e., the keyholing melt pool brings the nanodroplets downwards to the bottom of the melt pool. At the same time, the Marangoni convection flow pulls nanodroplets away from the center of the melt pool. This may help prevent the nanodroplets from merging during the PBF-LB/M process [61].

Further effects important to the dispersion and redistribution of the Ag nanodroplets, such as the capturing effects from the grain boundary during resolidification of the melt pool, should be investigated and discussed via droplet tracing simulations from additivated NPs in future studies. Furthermore, Martin et al. [31] demonstrated the effect of ZrH_2 and TiO_2 NPs aligning with the lattice of TiAl6V4 and Al7075 alloys, respectively, and attributing to an inducing low-energy-barrier epitaxial growth during the PBF-LB/M process. This, in turn, accelerates the solidification process and effectively restricts grain growth. But lattice mismatches induced by additional elements can cause distortions of the $Nd_2Fe_{14}B$ unit cell, which depend on the composition and orientation of the second phase [5]. Distortions at the interfaces between $Nd_2Fe_{14}B$ and Nd-rich phases can be > 1 nm [5], which could be referred to as the redistribution of surface energy [62]. These distortions can influence magnetic properties if they reduce the magnetocrystalline anisotropy of the $Nd_2Fe_{14}B$ unit cell, which is known for Nd-rich and oxide Nd_2O_3 grains. For instance, Woodcock and Gutfleisch [55] showed the presence of high defect densities in the Nd-rich phases using EBSD. Consequently, we investigated the samples via EBSD to analyze the influence on the grain size and orientation (see Figure 5C, D).

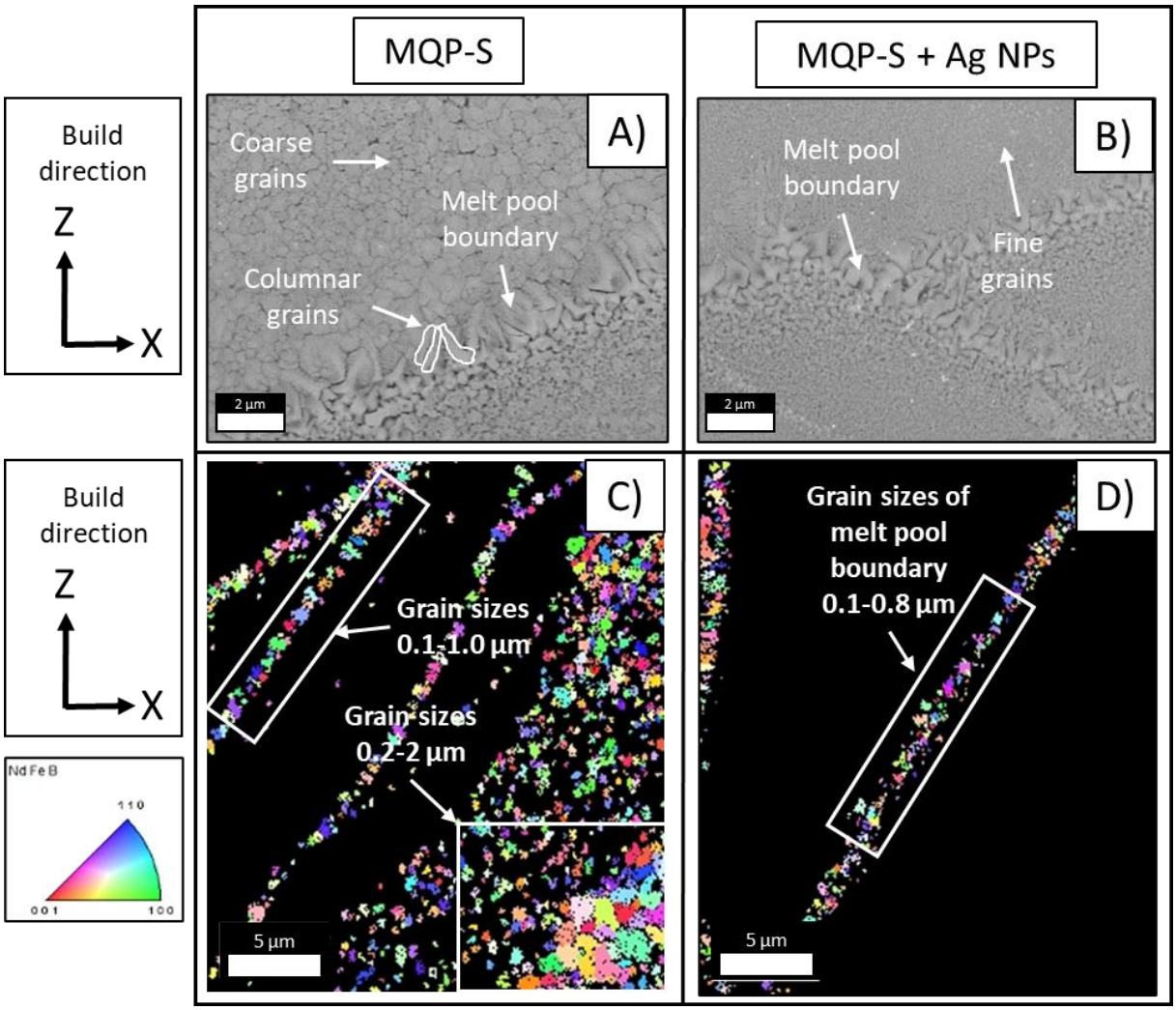

Figure 5 HR-SEM images at a magnification of 20,000x of A) a sample of pure MQP-S and B) a sample of MQP-S with the addition of 1 wt.% Ag NPs. Inverse pole figure (IPF) maps analyzed by EBSD at a magnification of 8,000x of C) pure MQP-S and D) MQP-S + 1 wt.% Ag after the PBF-LB/M process with a VED of 71.5 J/mm³. Cross-sections along the X-Z plane have been made, with the Z-axis resembling the build direction. The crystallographic orientations are indicated by the orientation legend for tetragonal symmetry.

Both microstructures of the PBF-LB-printed parts show non-indexed regions appearing black, which probably originate from nanocrystalline grains with grain sizes below the detection limit of EBSD (below 10 pixels) and have been excluded from the investigation here but are shown unmodified in Figure S7 in section 6 of the SI. The microstructure of unmodified MQP-S (Figure 5C) shows regions of fine grains in the melt pool boundary region in the size of roughly 0.1 – 1.0 µm and coarse grains in the range of roughly 0.2 – 2 µm size (see also Figure S8 in section 6 of the SI), which are orientated arbitrarily in all possible axis directions. In contrast, the microstructure of MQP-S modified with Ag NPs (Figure 5D) shows only some fine grains in the range of roughly 0.1 – 0.8 µm (raw data are given in Figure S9 in the SI), which are in the melt

pool boundary regions. Notably, the grains in the melt pool boundaries seem to be less or non-dendritic-elongated, which is different from the appearance in the BSE-SEM images in Figure 5A, B. This could be explained by the outer regions of the samples cooling down at higher speeds and leading to more equiaxed grains. In the core regions of samples, the heat transfer is lower and more impacted to cool at different gradients, but this requires further investigation.

A sample modified with Ag NPs has been analyzed via STEM, TEM-EDX, and HR-TEM, with the results shown in Figures S10-12 of section 6 in the SI. The STEM analysis revealed two regions, which can be differentiated by their grain sizes. The coarser region is in the range of a couple hundred nanometers but well below micrometer size. The region with finer grains is in the lower nanometer size. While the TEM-EDX did not show Ag, it could reveal the existence of two major phases, mainly the 2:14:1 phase and a ZrTi-rich grain boundary phase, which could be confirmed for both regions (with coarser and finer grains). At higher magnification, via HR-TEM, the 2:14:1 phase could be identified to be crystallites and the ZrTi-rich phase being amorphous. Another sample with 1 wt.% Ag NPs have been analyzed via atom probe tomography (APT), showing an even distribution of Fe, but a partial replacement of Nd by B in the outermost region of the reconstructed tip, while the Ag is evenly distributed with higher amounts of up to 10% in the outermost area of the tip.

Overall, the micro- and nanostructural analysis indicated that modifying the feedstock with Ag NPs shows an interesting microstructure with grain sizes potentially in the nanometer size range. This could either be the result of not fully molten MQP-S particles with exchange-coupled $Nd_2Fe_{14}B$ and α-Fe (as would be usual for conventionally produced MQP-S), or the powder is remolten but due to low power of the laser, the cooling rate of the pull is so fast, that the nanocrystalline structure reappears. While the first seems more likely, this requires further investigation.

Conclusion

Although laser powder bed fusion of metals is a mature additive manufacturing method with the potential to save material, particularly if those are made of critical elements, the 3D printing of permanent magnets based on commercial Nd-Fe-B-based micro powders is still in its infancy. Often, the hard magnetic phases are compromised or even lost during printing. The present study highlights the potential of modifying the surface of the powder feedstock material with low melting point nanoparticles to

improve the magnetic properties of Nd-Fe-B magnets fabricated through laser powder bed fusion at moderate volumetric energy densities. The study provides insights into the impact of laser parameters such as laser power and scan speed on part quality and as-built part density. While the part density increases with decreasing laser power and increasing scanning speed, the as-build parts show a drastic drop in functionality after processing with only 64.8 J/mm^3 (70 W, 3000 mm/s). It was found that increasing the laser power or decreasing the scan speed leads to greater heat accumulation at the beam spot, resulting in a more pronounced overheated region, which negatively impacts the part quality and reduces its density. While such overheated regions are likely to cause full melting of the microparticles, partial melting or sintering must be considered in the other regions. The best functional performance was reached after printing with 71.5 J/mm^3 (74 W, 2300 mm/s). The as-built parts show an interesting microstructure with grain sizes potentially in the nanometer size range. Here, we cannot differentiate whether we have not fully remelted MQPS particles with exchange-coupled $Nd_2Fe_{14}B$ and α-Fe or remelt the powder, but due to the low power of the laser source, the cooling rate of the pull is so fast that the nanocrystalline structures reappearing again. The former is more likely because the as-build parts show a density of < 90%, typical for (partial) sintering rather than full-melting conditions. While modifying the feedstock with Ag NPs shows a minor effect on the microstructure, it shows a huge impact on the functional properties. Note that also the unmodified feedstock shows an excellent performance with a coercivity of up to 769 $\pm$ 59 kA/m. The modified sample showed increased coercivity by up to 20% without negatively impacting the remanence.

Acknowledgments

This work was financially supported by the Deutsche Forschungsgemeinschaft (DFG, German Research Foundation) within the Collaborative Research Centre / Transregio (CRC/TRR) 270, Project ID No. 405553726, subprojects A01, A06, A08, A10, A11 and Z01, and within the priority program (SPP) 2122 “Materials for Additive Manufacturing (MATframe)”, project SE 2935/1-2. We thank Enrico Bruder of the Institute of Material Science at the Technical University of Darmstadt for support with the EBSD analysis. T. D. Oyedeji, Y. Yang, and B.-X. Xu greatly appreciate the access to the Lichtenberg II High-Performance Computer (HPC) and the technique supports from the HHLR, Technical University of Darmstadt. The computation time on the HPC is granted by the NHR4CES Resource Allocation Board under the project “special00007”. Further, we

would like to acknowledge Ying Yang and Matthias Miertz of the Department of Technical Chemistry I at the University of Duisburg-Essen for their support during nanoparticle production.

Conflicts of interest

The authors declare no conflicts.

References

[1] Gutfleisch, O.; Willard, M. A.; Brück, E.; Chen, C. H.; Sankar, S. G.; Liu, J. P. Magnetic Materials and Devices for the 21st Century: Stronger, Lighter, and More Energy Efficient. *Adv. Mater.*, **2011**, *23* (7), 821–842. https://doi.org/10.1002/adma.201002180.

[2] Coey, J. M. D. Perspective and Prospects for Rare Earth Permanent Magnets. *Engineering*, **2020**, *6* (2), 119–131. https://doi.org/10.1016/j.eng.2018.11.034.

[3] Skokov, K. P.; Gutfleisch, O. Heavy Rare Earth Free, Free Rare Earth and Rare Earth Free Magnets - Vision and Reality. *Scr. Mater.*, **2018**, *154*, 289–294. https://doi.org/10.1016/j.scriptamat.2018.01.032.

[4] Sagawa, M.; Fujimura, S.; Togawa, N.; Yamamoto, H.; Matsuura, Y. New Material for Permanent Magnets on a Base of Nd and Fe (Invited). *J. Appl. Phys.*, **1984**, *55* (6), 2083–2087. https://doi.org/10.1063/1.333572.

[5] Woodcock, T. G.; Zhang, Y.; Hrkac, G.; Ciuta, G.; Dempsey, N. M.; Schrefl, T.; Gutfleisch, O.; Givord, D. Understanding the Microstructure and Coercivity of High Performance NdFeB-Based Magnets. *Scr. Mater.*, **2012**, *67* (6), 536–541. https://doi.org/10.1016/j.scriptamat.2012.05.038.

[6] Hono, K.; Sepehri-Amin, H. Strategy for High-Coercivity Nd–Fe–B Magnets. *Scr. Mater.*, **2012**, *67* (6), 530–535. https://doi.org/10.1016/j.scriptamat.2012.06.038.

[7] Li, J.; Sepehri-Amin, H.; Sasaki, T.; Ohkubo, T.; Hono, K. Most Frequently Asked Questions about the Coercivity of Nd-Fe-B Permanent Magnets. *Sci. Technol. Adv. Mater.*, **2021**, *22* (1), 386–403. https://doi.org/10.1080/14686996.2021.1916377.

[8] Croat, J. J.; Herbst, J. F.; Lee, R. W.; Pinkerton, F. E. High-energy Product Nd-Fe-B Permanent Magnets. *Appl. Phys. Lett.*, **1984**, *44* (1), 148–149. https://doi.org/10.1063/1.94584.

[9] Mishra, R. K. Microstructure of Hot-pressed and Die-upset NdFeB Magnets. *J. Appl. Phys.*, **1987**, *62* (3), 967–971. https://doi.org/10.1063/1.339709.

[10] Mishra, R. K.; Chu, T.-Y.; Rabenberg, L. K. The Development of the Microstructure of Die-Upset Nd-Fe-B Magnets. *J. Magn. Magn. Mater.*, **1990**, *84* (1), 88–94. https://doi.org/10.1016/0304-8853(90)90168-P.

[11] Fuerst, C. D.; Brewer, E. G. Diffusion-alloyed Additives in Die-upset Nd-Fe-B Magnets. *J. Appl. Phys.*, **1991**, *69* (8), 5826–5828. https://doi.org/10.1063/1.347862.

[12] Kusoglu, I. M.; Huber, F.; Doñate-Buendía, C.; Rosa Ziefuss, A.; Gökce, B.; T. Sehrt, J.; Kwade, A.; Schmidt, M.; Barcikowski, S. Nanoparticle Additivation Effects on Laser Powder Bed Fusion of Metals and Polymers—A Theoretical Concept for an Inter-Laboratory Study Design All Along the Process Chain, Including Research Data Management. *Materials*, **2021**, *14* (17), 4892. https://doi.org/10.3390/ma14174892.

[13] Gu, D. D.; Meiners, W.; Wissenbach, K.; Poprawe, R. Laser Additive Manufacturing of Metallic Components: Materials, Processes and Mechanisms. *Int. Mater. Rev.*, **2012**, *57* (3), 133–164. https://doi.org/10.1179/1743280411Y.0000000014.

[14] King, W. E.; Anderson, A. T.; Ferencz, R. M.; Hodge, N. E.; Kamath, C.; Khairallah, S. A.; Rubenchik, A. M. Laser Powder Bed Fusion Additive Manufacturing of Metals; Physics, Computational, and Materials Challenges. *Appl. Phys. Rev.*, **2015**, *2* (4), 041304. https://doi.org/10.1063/1.4937809.

[15] Frazier, W. E. Metal Additive Manufacturing: A Review. *J. Mater. Eng. Perform.*, **2014**, *23* (6), 1917–1928. https://doi.org/10.1007/s11665-014-0958-z.

[16] Wu, J.; Aboulkhair, N. T.; Degano, M.; Ashcroft, I.; Hague, R. J. M. Process-Structure-Property Relationships in Laser Powder Bed Fusion of Permanent Magnetic Nd-Fe-B. *Mater. Des.*, **2021**, *209*, 109992. https://doi.org/10.1016/j.matdes.2021.109992.

[17] Jaćimović, J.; Binda, F.; Herrmann, L. G.; Greuter, F.; Genta, J.; Calvo, M.; Tomše, T.; Simon, R. A. Net Shape 3D Printed NdFeB Permanent Magnet. *Adv. Eng. Mater.*, **2017**, *19* (8), 1700098. https://doi.org/10.1002/adem.201700098.

[18] Urban, N.; Meyer, A.; Keller, V.; Franke, J. Contribution of Additive Manufacturing of Rare Earth Material to the Increase in Performance and Resource Efficiency of Permanent Magnets. *Appl. Mech. Mater.*, **2018**, *882*, 135–141. https://doi.org/10.4028/www.scientific.net/AMM.882.135.

[19] Skalon, M.; Görtler, M.; Meier, B.; Arneitz, S.; Urban, N.; Mitsche, S.; Huber, C.; Franke, J.; Sommitsch, C. Influence of Melt-Pool Stability in 3D Printing of NdFeB Magnets on Density and Magnetic Properties. *Materials*, **2020**, *13* (1), 139. https://doi.org/10.3390/ma13010139.

[20] Huber, C.; Sepehri-Amin, H.; Goertler, M.; Groenefeld, M.; Teliban, I.; Hono, K.; Suess, D. Coercivity Enhancement of Selective Laser Sintered NdFeB Magnets by Grain Boundary Infiltration. *Acta Mater.*, **2019**, *172*, 66–71. https://doi.org/10.1016/j.actamat.2019.04.037.

[21] Goll, D.; Trauter, F.; Bernthaler, T.; Schanz, J.; Riegel, H.; Schneider, G. Additive Manufacturing of Bulk Nanocrystalline FeNdB Based Permanent Magnets. *Micromachines*, **2021**, *12* (5), 538. https://doi.org/10.3390/mi12050538.

[22] Bittner, F.; Thielsch, J.; Drossel, W.-G. Laser Powder Bed Fusion of Nd–Fe–B Permanent Magnets. *Prog. Addit. Manuf.*, **2020**, *5* (1), 3–9. https://doi.org/10.1007/s40964-020-00117-7.

[23] Tosoni, O.; Borges, E.; Reijonen, J.; Antikainen, A.; Schaefer, L.; Riegg, S.; Gutfleisch, O. High-Coercivity Copper-Rich Nd-Fe-B Magnets by Powder Bed Fusion Using Laser Beam Method. **2023**. https://doi.org/10.2139/ssrn.4149170.

[24] Jian, W.-Y. J.; Cheng, C.-W.; Chang, W.-C.; Huang, T.-Y.; Liang, Y.-C.; Lee, A.-C.; Chang, T.-W.; Tsai, M.-C. Fabrication of Crack-Free Nd-Fe-B Magnets with Laser Powder Bed Fusion. *Materialia*, **2022**, *21*, 101351. https://doi.org/10.1016/j.mtla.2022.101351.

[25] Volegov, A. S.; Andreev, S. V.; Selezneva, N. V.; Ryzhikhin, I. A.; Kudrevatykh, N. V.; Mädler, L.; Okulov, I. V. Additive Manufacturing of Heavy Rare Earth Free High-Coercivity Permanent Magnets. *Acta Mater.*, **2020**, *188*, 733–739. https://doi.org/10.1016/j.actamat.2020.02.058.

[26] Bittner, F.; Thielsch, J.; Drossel, W.-G. Microstructure and Magnetic Properties of Nd-Fe-B Permanent Magnets Produced by Laser Powder Bed Fusion. *Scr. Mater.*, **2021**, *201*, 113921. https://doi.org/10.1016/j.scriptamat.2021.113921.

[27] Bittner, F.; Thielsch, J.; Drossel, W.-G. Unexpected Coercivity Enhancement >1T for Nd-Fe-B Permanent Magnets With 20 Wt% Nd Produced by Laser Powder Bed Fusion. *IEEE Trans. Magn.*, **2022**, *58* (9), 1–5. https://doi.org/10.1109/TMAG.2022.3167246.

[28] Huber, C.; Mitteramskogler, G.; Goertler, M.; Teliban, I.; Groenefeld, M.; Suess, D. Additive Manufactured Isotropic NdFeB Magnets by Stereolithography, Fused Filament Fabrication, and Selective Laser Sintering. arXiv November 7, 2019. https://doi.org/10.48550/arXiv.1911.02881.

[29] Sridharan, N.; Cakmak, E.; List, F. A.; Ucar, H.; Constantinides, S.; Babu, S. S.; McCall, S. K.; Paranthaman, M. P. Rationalization of Solidification Mechanism of Nd–Fe–B Magnets during Laser Directed-Energy Deposition. *J. Mater. Sci.*, **2018**, *53* (11), 8619–8626. https://doi.org/10.1007/s10853-018-2178-7.

[30] Magnequench Inc. Material Data Sheet of MQP-S, 2006.

[31] Martin, J. H.; Yahata, B. D.; Hundley, J. M.; Mayer, J. A.; Schaedler, T. A.; Pollock, T. M. 3D Printing of High-Strength Aluminium Alloys. *Nature*, **2017**, *549* (7672), 365–369. https://doi.org/10.1038/nature23894.

[32] Rumpf, H. Die Wissenschaft des Agglomerierens. *Chem. Ing. Tech.*, **1974**, *46* (1), 1–11. https://doi.org/10.1002/cite.330460102.

[33] Meyer, K.; Zimmermann, I. Effect of Glidants in Binary Powder Mixtures. *Powder Technol.*, **2004**, *139* (1), 40–54. https://doi.org/10.1016/j.powtec.2003.09.007.

[34] Letzel, A.; Maurer, E.; Meixner, M.; Poprawe, R.; Stollenwerk, J.; Hessner, S.; Lehmann, K.; Gökce, B.; Barcikowski, S. Effect of Various Dispersing Agents on the Stability of Silver Microparticle Dispersion and the Formulation of Uniform Silver Film by Laser Melting. *J. Laser Appl.*, **2016**, *28* (4), 042004. https://doi.org/10.2351/1.4955011.

[35] Zhang, D.; Gökce, B.; Barcikowski, S. Laser Synthesis and Processing of Colloids: Fundamentals and Applications. *Chem. Rev.*, **2017**, *117* (5), 3990–4103. https://doi.org/10.1021/acs.chemrev.6b00468.

[36] Zhao, T. S.; Kim, Y. B.; Jeung, W. Y. Magnetic Properties and Microstructure of NdFeB Sintered Magnets by the Addition of Ag Powder. *IEEE Trans. Magn.*, **2000**, *36* (5), 3318–3320. https://doi.org/10.1109/20.908784.

[37] Chen, H.; Yang, X.; Sun, L.; Yu, P.; Zhang, X.; Luo, L. Effects of Ag on the Magnetic and Mechanical Properties of Sintered NdFeB Permanent Magnets. *J. Magn. Magn. Mater.*, **2019**, *485*, 49–53. https://doi.org/10.1016/j.jmmm.2019.04.071.

[38] Zhang, H.; Yang, X.; Bai, S.; Chen, K.; Ye, F. Toughness of Sintered NdFeB Magnets. *J. Iron Steel Res. Int.*, **2006**, *13*, 494–499. https://doi.org/10.1016/S1006-706X(08)60237-X.

[39] Onbattuvelli, V. P.; Enneti, R. K.; Park, S.-J.; Atre, S. V. The Effects of Nanoparticle Addition on SiC and AlN Powder–Polymer Mixtures: Packing and Flow Behavior. *Int. J. Refract. Met. Hard Mater.*, **2013**, *36*, 183–190. https://doi.org/10.1016/j.ijrmhm.2012.08.014.

[40] Streubel, R.; Barcikowski, S.; Gökce, B. Continuous Multigram Nanoparticle Synthesis by High-Power, High-Repetition-Rate Ultrafast Laser Ablation in Liquids. *Opt. Lett.*, **2016**, *41* (7), 1486–1489. https://doi.org/10.1364/OL.41.001486.

[41] Streubel, R.; Bendt, G.; Gökce, B. Pilot-Scale Synthesis of Metal Nanoparticles by High-Speed Pulsed Laser Ablation in Liquids. *Nanotechnology*, **2016**, *27* (20), 205602. https://doi.org/10.1088/0957-4484/27/20/205602.

[42] Rehbock, C.; Merk, V.; Gamrad, L.; Streubel, R.; Barcikowski, S. Size Control of Laser-Fabricated Surfactant -Free Gold Nanoparticles with Highly Diluted Electrolytes and Their Subsequent Bioconjugation. *Phys. Chem. Chem. Phys.*, **2013**, *15* (9), 3057–3067. https://doi.org/10.1039/C2CP42641B.

[43] Scipioni Bertoli, U.; Wolfer, A. J.; Matthews, M. J.; Delplanque, J.-P. R.; Schoenung, J. M. On the Limitations of Volumetric Energy Density as a Design Parameter for Selective Laser Melting. *Mater. Des.*, **2017**, *113*, 331–340. https://doi.org/10.1016/j.matdes.2016.10.037.

[44] Caiazzo, F.; Alfieri, V.; Casalino, G. On the Relevance of Volumetric Energy Density in the Investigation of Inconel 718 Laser Powder Bed Fusion. *Materials*, **2020**, *13* (3), 538. https://doi.org/10.3390/ma13030538.

[45] Urban, N.; Huber, F.; Franke, J. Influences of Process Parameters on Rare Earth Magnets Produced by Laser Beam Melting. In *2017 7th International Electric Drives Production Conference (EDPC)*; 2017; pp 1–5. https://doi.org/10.1109/EDPC.2017.8328149.

[46] Kusoglu, I. M.; Vieth, P.; Heiland, S.; Huber, F.; Lüddecke, A.; Ziefuss, A. R.; Kwade, A.; Schmidt, M.; Schaper, M.; Barcikowski, S.; et al. Microstructure and Corrosion Properties of PBF-LB Produced Carbide Nanoparticles Additivated AlSi10Mg Parts. *Procedia CIRP*, **2022**, *111*, 10–13. https://doi.org/10.1016/j.procir.2022.08.046.

[47] Brown, C. U.; Jacob, G.; Possolo, A.; Beauchamp, C.; Peltz, M.; Stoudt, M.; Donmez, A. *The Effects of Laser Powder Bed Fusion Process Parameters on Material Hardness and Density for Nickel Alloy 625*; NIST AMS 100-19; National Institute of Standards and Technology: Gaithersburg, MD, 2018; p NIST AMS 100-19. https://doi.org/10.6028/NIST.AMS.100-19.

[48] Paraschiv, A.; Matache, G.; Condruz, M. R.; Frigioescu, T. F.; Pambaguian, L. Laser Powder Bed Fusion Process Parameters' Optimization for Fabrication of Dense IN 625. *Materials*, **2022**, *15* (16), 5777. https://doi.org/10.3390/ma15165777.

[49] Yang, Y.; Großmann, A.; Kühn, P.; Mölleney, J.; Kropholler, L.; Mittelstedt, C.; Xu, B.-X. Validated Dimensionless Scaling Law for Melt Pool Width in Laser Powder Bed Fusion. *J. Mater. Process. Technol.*, **2022**, *299*, 117316. https://doi.org/10.1016/j.jmatprotec.2021.117316.

[50] Khairallah, S. A.; Martin, A. A.; Lee, J. R. I.; Guss, G.; Calta, N. P.; Hammons, J. A.; Nielsen, M. H.; Chaput, K.; Schwalbach, E.; Shah, M. N.; et al. Controlling Interdependent Meso-Nanosecond Dynamics and Defect Generation in Metal 3D Printing. *Science*, **2020**, *368* (6491), 660–665. https://doi.org/10.1126/science.aay7830.

[51] Khairallah, S. A.; Anderson, A. Mesoscopic Simulation Model of Selective Laser Melting of Stainless Steel Powder. *J. Mater. Process. Technol.*, **2014**, *214* (11), 2627–2636. https://doi.org/10.1016/j.jmatprotec.2014.06.001.

[52] Yang, Y.; Großmann, A.; Kühn, P.; Mölleney, J.; Kropholler, L.; Mittelstedt, C.; Xu, B.-X. Validated Dimensionless Scaling Law for Melt Pool Width in Laser Powder Bed Fusion. *J. Mater. Process. Technol.*, **2022**, *299*, 117316. https://doi.org/10.1016/j.jmatprotec.2021.117316.

[53] Cheng, B.; Chou, K. A Numerical Investigation of Thermal Property Effects on Melt Pool Characteristics in Powder-Bed Electron Beam Additive Manufacturing. *Proc. Inst. Mech. Eng. Part B J. Eng. Manuf.*, **2018**, *232* (9), 1615–1627. https://doi.org/10.1177/0954405416673105.

[54] Ding, X.; Koizumi, Y.; Wei, D.; Chiba, A. Effect of Process Parameters on Melt Pool Geometry and Microstructure Development for Electron Beam Melting of IN718: A Systematic Single Bead Analysis Study. *Addit. Manuf.*, **2019**, *26*, 215–226. https://doi.org/10.1016/j.addma.2018.12.018.

[55] Woodcock, T. G.; Gutfleisch, O. Multi-Phase EBSD Mapping and Local Texture Analysis in NdFeB Sintered Magnets. *Acta Mater.*, **2011**, *59* (3), 1026–1036. https://doi.org/10.1016/j.actamat.2010.10.033.

[56] Suzuki, S.; Kuno, T.; Urushibata, K.; Kobayashi, K.; Sakuma, N.; Washio, K.; Kishimoto, H.; Kato, A.; Manabe, A. A (Nd, Zr)(Fe, Co)11.5Ti0.5Nx Compound as a Permanent Magnet Material. *AIP Adv.*, **2014**, *4* (11), 117131. https://doi.org/10.1063/1.4902176.

[57] Pannitz, O.; Sehrt, J. T. Transferability of Process Parameters in Laser Powder Bed Fusion Processes for an Energy and Cost Efficient Manufacturing. *Sustainability*, **2020**, *12* (4), 1565. https://doi.org/10.3390/su12041565.

[58] Gutfleisch, O. Controlling the Properties of High Energy Density Permanent Magnetic Materials by Different Processing Routes. *J. Phys. Appl. Phys.*, **2000**, *33* (17), R157. https://doi.org/10.1088/0022-3727/33/17/201.

[59] Khairallah, S. A.; Anderson, A. T.; Rubenchik, A.; King, W. E. Laser Powder-Bed Fusion Additive Manufacturing: Physics of Complex Melt Flow and Formation Mechanisms of Pores, Spatter, and Denudation Zones. *Acta Mater.*, **2016**, *108*, 36–45. https://doi.org/10.1016/j.actamat.2016.02.014.
[60] Front Matter. In *Intermolecular and Surface Forces (Third Edition)*; Israelachvili, J. N., Ed.; Academic Press: San Diego, 2011; p iii. https://doi.org/10.1016/B978-0-12-375182-9.10025-9.
[61] Doñate-Buendia, C.; Kürnsteiner, P.; Stern, F.; Wilms, M. B.; Streubel, R.; Kusoglu, I. M.; Tenkamp, J.; Bruder, E.; Pirch, N.; Barcikowski, S.; et al. Microstructure Formation and Mechanical Properties of ODS Steels Built by Laser Additive Manufacturing of Nanoparticle Coated Iron-Chromium Powders. *Acta Mater.*, **2021**, *206*, 116566. https://doi.org/10.1016/j.actamat.2020.116566.
[62] Yuan, X.; Zhu, J. Misorientations across Boundary Planes in a Sintered NdFeB Permanent Magnet. *RSC Adv.*, **2022**, *12* (31), 20412–20422. https://doi.org/10.1039/D2RA01670B.
[63] Yang, Y.; Oyedeji, T. D.; Kühn, P.; Xu, B.-X. Investigation on Temperature-Gradient-Driven Effects in Unconventional Sintering via Non-Isothermal Phase-Field Simulation. *Scr. Mater.*, **2020**, *186*, 152–157. https://doi.org/10.1016/j.scriptamat.2020.05.016.
[64] Yang, Y.; Ragnvaldsen, O.; Bai, Y.; Yi, M.; Xu, B.-X. 3D Non-Isothermal Phase-Field Simulation of Microstructure Evolution during Selective Laser Sintering. *Npj Comput. Mater.*, **2019**, *5* (1), 1–12. https://doi.org/10.1038/s41524-019-0219-7.
[65] Yang, Y.; Oyedeji, T. D.; Zhou, X.; Albe, K.; Xu, B.-X. Tailoring Magnetic Hysteresis of Fe-Ni Permalloy by Additive Manufacturing: Multiphysics-Multiscale Simulations of Process-Property Relationships. arXiv February 4, 2023. https://doi.org/10.48550/arXiv.2302.02217.
[66] Yang, Y.; Kühn, P.; Yi, M.; Egger, H.; Xu, B.-X. Non-Isothermal Phase-Field Modeling of Heat–Melt–Microstructure-Coupled Processes During Powder Bed Fusion. *JOM*, **2020**, *72* (4), 1719–1733. https://doi.org/10.1007/s11837-019-03982-y.
[67] Permann, C. J.; Gaston, D. R.; Andrš, D.; Carlsen, R. W.; Kong, F.; Lindsay, A. D.; Miller, J. M.; Peterson, J. W.; Slaughter, A. E.; Stogner, R. H.; et al. MOOSE: Enabling Massively Parallel Multiphysics Simulation. *SoftwareX*, **2020**, *11*, 100430. https://doi.org/10.1016/j.softx.2020.100430.
[68] Tonks, M. R.; Gaston, D.; Millett, P. C.; Andrs, D.; Talbot, P. An Object-Oriented Finite Element Framework for Multiphysics Phase Field Simulations. *Comput. Mater. Sci.*, **2012**, *51* (1), 20–29. https://doi.org/10.1016/j.commatsci.2011.07.028.
[69] Yang, Y.; Ragnvaldsen, O.; Bai, Y.; Yi, M.; Xu, B.-X. 3D Non-Isothermal Phase-Field Simulation of Microstructure Evolution during Selective Laser Sintering. *Npj Comput. Mater.*, **2019**, *5* (1), 81. https://doi.org/10.1038/s41524-019-0219-7.
[70] Rong, C.; Shen, B. Nanocrystalline and Nanocomposite Permanent Magnets by Melt Spinning Technique. *Chin. Phys. B*, **2018**, *27* (11), 117502. https://doi.org/10.1088/1674-1056/27/11/117502.
[71] neorem, magnets. Characteristic Physical Properties of Sintered NdFeB Magnet Material at 20°C, 2018.
[72] Valencia, J. J.; Quested, P. N. Thermophysical Properties. In *Casting, Vol 15, ASM Handbook, ASM International*; 2013.
[73] Blakely, J. M.; Mykura, H. Studies of Vacuum Annealed Iron Surfaces. *Acta Metall.*, **1963**, *11* (5), 399–404. https://doi.org/10.1016/0001-6160(63)90164-0.
[74] Mead, H. W.; Birchenall, C. E. Self-Diffusion of Iron In Austenite. *JOM*, **1956**, *8* (10), 1336–1339. https://doi.org/10.1007/BF03377878.
[75] Price, A. T.; Holl, H. A.; Greenough, A. P. The Surface Energy and Self Diffusion Coefficient of Solid Iron above 1350°C. *Acta Metall.*, **1964**, *12* (1), 49–58. https://doi.org/10.1016/0001-6160(64)90053-7.
[76] Liu, F. R.; Zhang, Q.; Zhou, W. P.; Zhao, J. J.; Chen, J. M. Micro Scale 3D FEM Simulation on Thermal Evolution within the Porous Structure in Selective Laser Sintering. *J. Mater. Process. Technol.*, **2012**, *212* (10), 2058–2065. https://doi.org/10.1016/j.jmatprotec.2012.05.010.
[77] Schäfer, L.; Skokov, K.; Liu, J.; Maccari, F.; Braun, T.; Riegg, S.; Radulov, I.; Gassmann, J.; Merschroth, H.; Harbig, J.; et al. Design and Qualification of Pr–Fe–Cu–B Alloys for the Additive Manufacturing of Permanent Magnets. *Adv. Funct. Mater.*, **2021**, *31* (33), 2102148. https://doi.org/10.1002/adfm.202102148.
[78] Goll, D.; Trauter, F.; Loeffler, R.; Gross, T.; Schneider, G. Additive Manufacturing of Textured FePrCuB Permanent Magnets. *Micromachines*, **2021**, *12* (9), 1056. https://doi.org/10.3390/mi12091056.